

Supporting Information for

**Leveraging surface phonon polaritons for enhanced Q -factor
of mid-infrared BaTiO₃ nanoresonators**

TAO CHENG¹, HUANHUAN ZHAO², WEIHENG KONG³, LINHUA LIU^{1,2*}, AND
JIA-YUE YANG^{1,2*}

¹*Optics & Thermal Radiation Research Center, Institute of Frontier and Interdisciplinary Science, Shandong University, Qingdao, 266237, P. R. China*

²*School of Energy and Power Engineering, Shandong University, Jinan, 250061, P. R. China*

³*Science and Technology Research Center of China Customs, Beijing 100026, P.R. China*

S1. Crystal structure of tetragonal BaTiO₃ (BTO) wafers with (001) and (100) crystal orientations

The (100) crystal orientation and (100) crystal orientation BTO wafers were characterized by x-ray diffraction XRD (X'Pert PRO) with Cu K_{α1} irradiation at a scanning rate of 2°/min with 2θ ranging from 20° to 50°. They have the same patterns, but the broadening of the peaks in the (001) crystal orientation is slightly wider than those in the (100) crystal orientation. They both show diffraction peaks at 2θ = 22.04° (22.08°), 22.31° (22.33°), 44.86° (44.81°), and 45.39° (45.31°) corresponding to the planes of (001), (100), (002), and (200), respectively. The presence of peaks of (002) and (200) at 2θ ≈ 45° confirm that the BTO wafers are in a tetragonal ferroelectric phase².

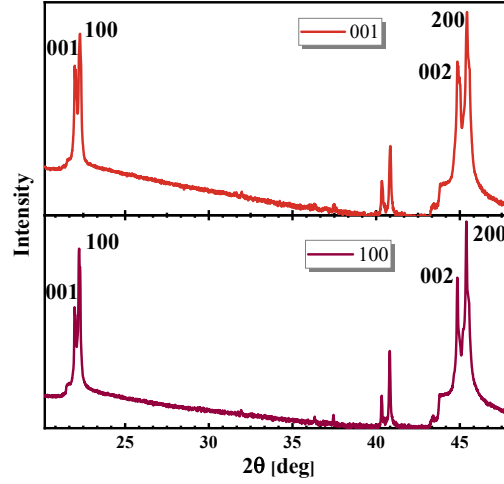


Figure S1. XRD patterns of (001) and (100) crystal orientation BTO wafers.

S2. Comparison of BaTiO₃ anisotropic dielectric function with literature

The experimentally measured BTO anisotropic dielectric function as a function of wavelength is given in Figure S1(a). Figure S1(b) shows the results of experimentally obtained (100) crystal-oriented dielectric functions (ϵ_{yy} and ϵ_{zz}) in comparison with the literature³.

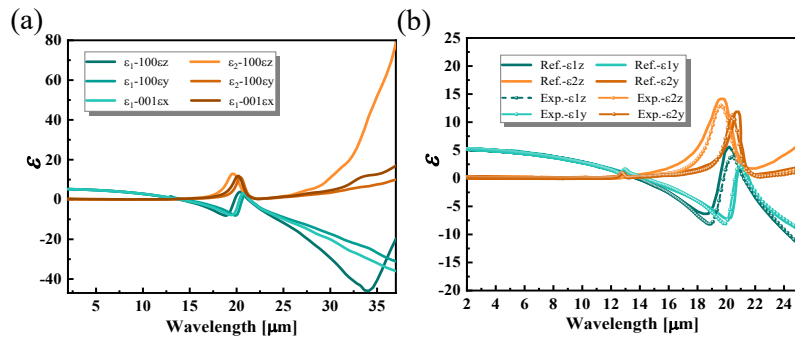


Figure S2. BTO anisotropic dielectric function as a function of wavelength. (a) Dielectric function of BTO in three directions. (b) Comparison of the dielectric function of BTO in 100ez and 100ey directions for (100) crystal orientations with literature results³.

S3. Etching process and characterization results of BTO microstructures

To fabricate the BTO metasurface, BTO ((001) and (100)) single crystals with dimensions of 5 mm×5 mm×0.5 mm were first cleaned using acetone solution and deionized water. A 100 nm chromium (Cr) layer was deposited as a hard etch mask. After that, a photoresist protective layer was applied. Then, the developer and etch steps

were carried out. A Heidelberg MLA150 model photolithography machine was selected, and the gases filled during the etching process were Trifluoromethane (CHF_3) and Argon (Ar). Finally, the BTO all-dielectric metasurfaces were obtained. Then, we characterized the metastructures' surface with the scanning electron microscope (SEM) model SU8220, choosing an inclination angle of 45° for the shot, as shown in Figure S3. It can be seen that the microstructures show a lovely periodic arrangement, but the shapes are not very uniform, and the heights are shallow. According to the output parameters of the software attached to the lithography machine, the long axis (Y) of the microstructures is $3.7 \mu\text{m}$, the short axis (X) is $1.6 \mu\text{m}$, the period of the microstructures is $8.5 \mu\text{m}$ and the height (h) is not uniform and is around $48 \text{ nm} - 58 \text{ nm}$. The reason for the uneven molding of the microstructure and the low height value is that the hardness of the single crystal is not easy to etch. The combination of gases chosen is not suitable, which can be considered to be replaced by octafluoropropane (C_3F_8)⁴ and Ar at a later stage to get the enhancement. Although the etching effect is not satisfactory, it can still help us to achieve the research purpose of confirming that the BTO super-surface can enhance absorption.

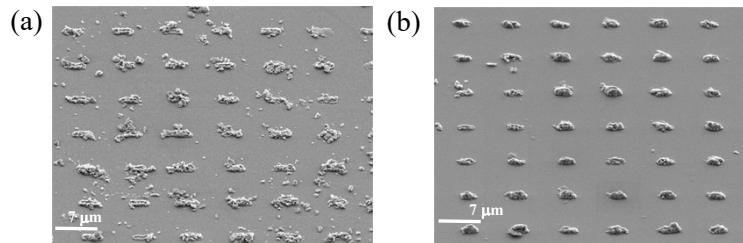


Figure S3. Scanning electron micrographs of BTO microstructures in the (a) (001) and (b) (100) crystal-orientations

S4. Mechanistic study of absorption differences between BTO single crystals and microstructures

Subsequently, we etched the BTO metasurfaces to study their impact on light modulation. The details of the etching process and scanning electron microscopy (SEM) results are shown in Section S3. Figures S4(a) and S4(b) show that the metasurfaces effectively reduce the reflectance and enhance the optical absorptance in all directions, despite the minimal etch height ($\approx 50 \text{ nm}$).

Additionally, Figures S4(c) and S4(d) show that the reflectance of both BTO wafers and metasurfaces in the TM polarization direction is lower than that in the transverse electric (TE) polarization direction at 65° oblique incidence angle. Figure 4(c) shows that the reflectance of the metasurfaces in the 001ey direction is weakest in the TM direction, while it is strongest in the TE direction for the 001ex direction. Notably, Figure 4(d) shows that in the TM (or TE) direction, the reflectance of the substrate wafer in the 100ez direction is the weakest, in contrast to the reflectance at perpendicular incidence, where the metasurfaces consistently exhibit weaker reflectance than the substrate. Moreover, the reflectance of the structure under oblique incidence within the Reststrahlen band is more consistently contrasting, unlike the varying reflectance at perpendicular incidence in different spectral intervals. In brief, even a metasurface with a modest etch height can substantially amplify its ability to modulate light.

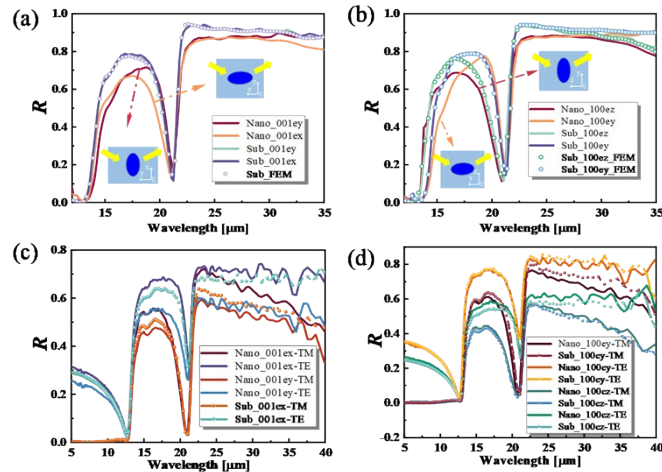


Figure S4. The reflectance of bulk BTO and all-dielectric metasurfaces at vertical incidence (TM polarization) were obtained from SE measurement in the (a) (001) crystal orientation and (b) (100) crystal orientation. The abbreviation “Nano_001ex” denotes the reflectance of the microstructure in the 001ex direction, the acronym “Sub_001ex” denotes the reflectance of the substrate structure in the 001ex direction, and so on. The solid lines represent the experimental measurements and the scattered lines represent the FEM calculations. The arrow-pointing insets indicate the schematic diagram of the test structure and the orientation axis for this case. The reflectance of

BTO bulk crystals and all-dielectric metasurfaces at 65° oblique incidence (TE and TM polarization) obtained from SE measurement in the (c) (001) crystal orientation and (d) (100) crystal orientation.

S5 Verification of the accuracy of FEM and FDTD calculations

Figure S5 compares the FEM calculation results with the FDTD calculation results for oblique incidence angles of 20° . The reflection amplitude calculated by FEM is smaller than that of FDTD, due to inherent differences and errors in both methods, especially under oblique incidence. Despite this, the absorption peak positions calculated by both methods align perfectly, ensuring the correctness of the theoretical analysis of the localized surface phonon polarization modes (LSPHs) in the main text. In conclusion, our theoretical calculations are accurate.

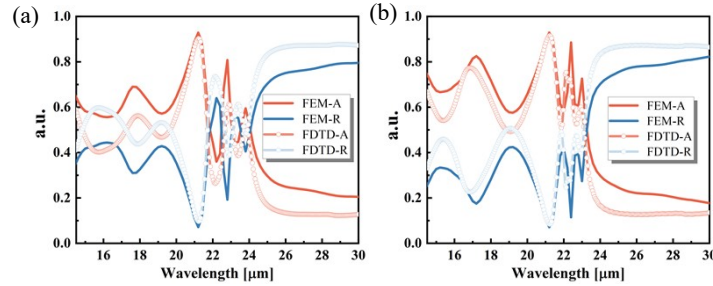


Figure S5. Validation of FDTD and FEM calculations for (001) crystal orientation

BTO under different parameters. Comparison of reflectance and absorptance at oblique incidence angle of 20° with structure parameters of (a) $X = 3 \mu\text{m}$, $Y = 1.5 \mu\text{m}$ and (b) $X = 3 \mu\text{m}$, $Y = 3 \mu\text{m}$.

S6 Normalized optical fields ($|E/E_0|$) and current density distributions in the $100ey$ direction and $100ez$ direction.

We compare the optical field and current density distributions in the other two structural directions. It is found that the optical field intensities of modes A, C, and D are highest in the $100ey$ direction and lowest (modes C and D) in the $100ez$ direction.

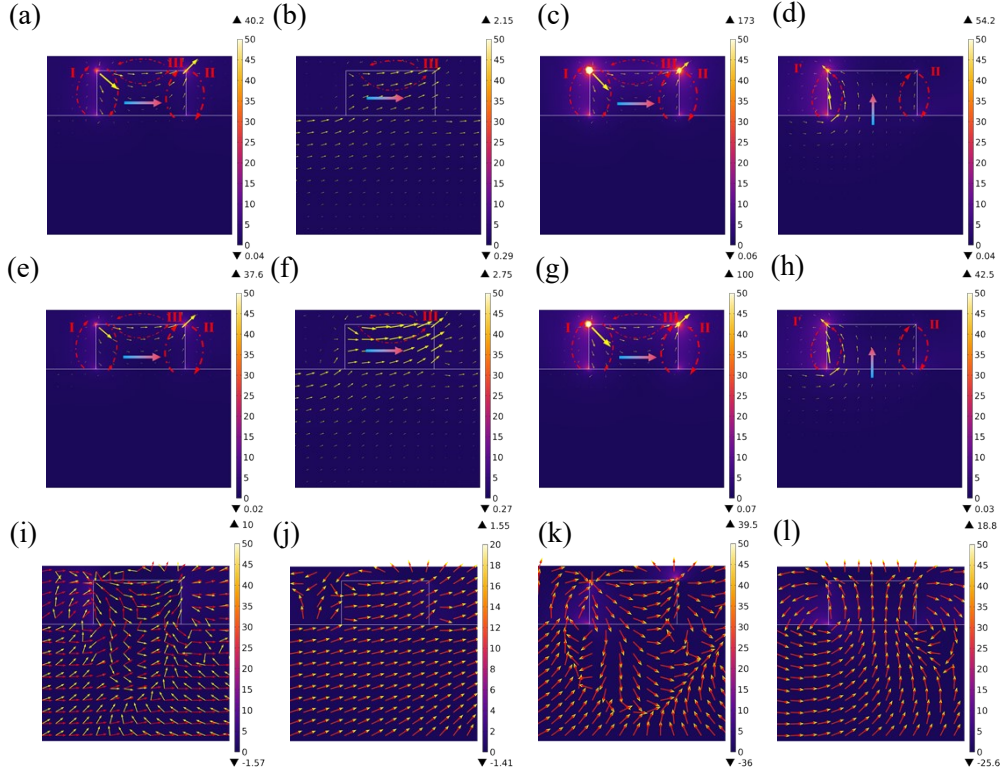


Figure S6. Normalized optical fields ($|E/E_0|$) and current density distributions in the 100ey direction in (a) mode A ($\lambda = 17.8 \mu\text{m}$), (b) mode B ($\lambda = 21.4 \mu\text{m}$), (c) mode C ($\lambda = 22.4 \mu\text{m}$), and (d) mode D ($\lambda = 23.2 \mu\text{m}$). Normalized optical fields ($|E/E_0|$) and current density distributions in the 100ez direction in (e) mode A ($\lambda = 17.2 \mu\text{m}$), (f) mode B ($\lambda = 21.4 \mu\text{m}$), (g) mode C ($\lambda = 22.4 \mu\text{m}$), and (h) mode D ($\lambda = 23.2 \mu\text{m}$). The yellow arrow indicates a proportional current density, i.e., the size of the arrow reflects the strength of the current density. The red circle is a magnified current circuit. The direction of the gradient-colored arrows points to the direction of the main body of current in the meta-atom. Normalized optical field ($|E/E_0|$) and current density distribution in the x-z plane in 001ex direction of (i) mode A, (j) mode B, (k) mode C, and (l) mode D. The yellow arrows and red arrows indicate the normalized current vector and the normalized electric field vector, respectively.

S7 Confirmation of the coupling of mode C and mode D into a single mode

Observing the surface charge density, there is a break in the dipole character at the upper surface of the structure of the E_x , E_y mode, i.e., the negative charge is more

dominant than the positive one. However, it can be seen from the complementary current density distribution that they are still TD1 modes. Therefore, by comparing the surface charge density distributions and current density distributions of the coupled modes E_R , E_X , E_Y , E_P , E_h with those of mode C, it is found that the coupled modes are all TD1 modes, and all are similar to mode C.

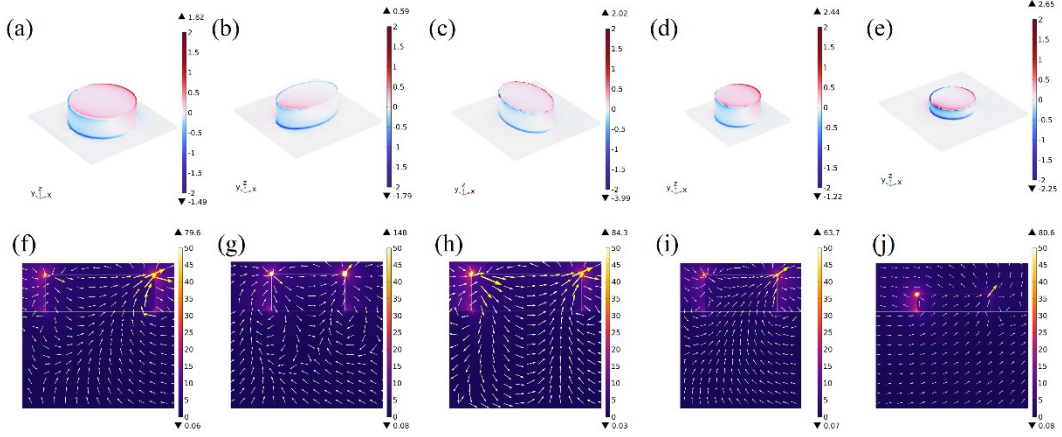


Figure S7. Surface charge density distribution of (a) mode E_R ($R = 4.5 \mu\text{m}$), (b) mode E_X ($X = 4.5 \mu\text{m}$), (c) mode E_Y ($Y = 4.5 \mu\text{m}$), (d) mode E_P ($P = 5 \mu\text{m}$), (e) mode E_h ($h = 0.7 \mu\text{m}$). Normalized optical fields ($|E/E_0|$) and current density distribution of (f) mode E_R ($R = 4.5 \mu\text{m}$), (g) mode E_X ($X = 4.5 \mu\text{m}$), (h) mode E_Y ($Y = 4.5 \mu\text{m}$), (i) mode E_P ($P = 5 \mu\text{m}$), (j) mode E_h ($h = 0.7 \mu\text{m}$).

S8 Enlarged view of localized modes E and A

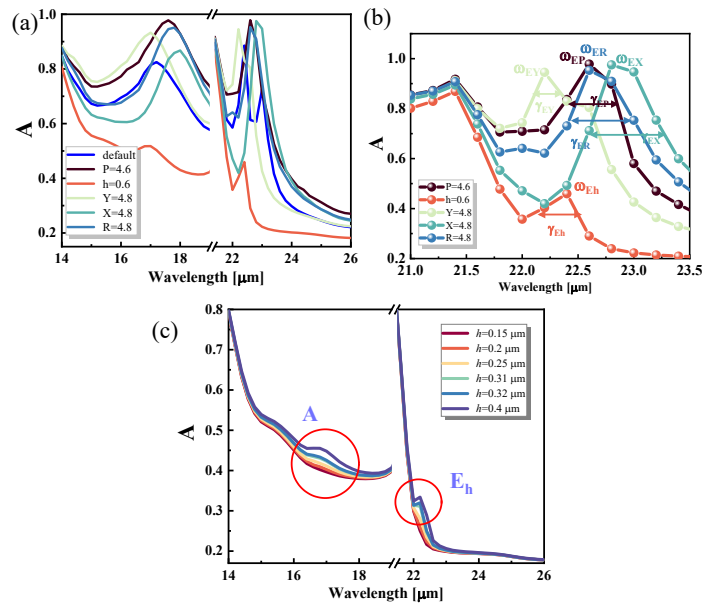


Figure S8 (a) Spectra at each geometric parameter when mode E reaches the steady state. (b) Individual spectra with the labels ω_i and γ_i . (c) Height dependence of local modes A and E.

Table S1 The values of ω_i and γ_i when mode E reaches the steady state

Parameters	Mode	ω_i (cm ⁻¹)	γ_i (cm ⁻¹)
Default	Mode C	446.23	3.90
	Mode D	434.22	5.13
P = 4.6 μ m	Mode E _P	442.48	10.77
H = 0.6 μ m	Mode E _h	446.43	6.2577
R = 4.8 μ m	Mode E _R	442.48	12.316
X = 4.8 μ m	Mode E _X	438.60	12.825
Y = 4.8 μ m	Mode E _Y	450.48	4.41

S9 Surface charge density distribution of mode E_R, mode E_X, and mode E_Y

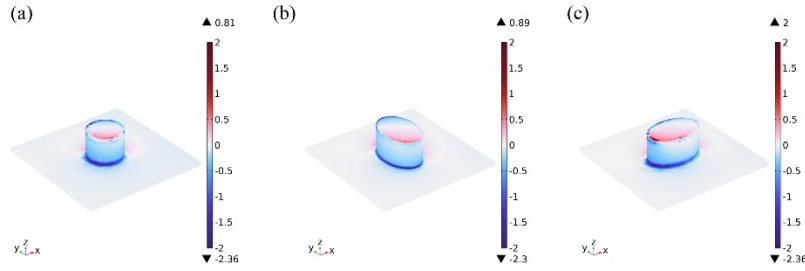


Figure S9. Surface charge density distribution of (a) mode E_R ($R = 2 \mu$ m), (b) mode E_X ($X = 2 \mu$ m), (c) mode E_Y ($Y = 2 \mu$ m)

S10 Surface charge density of modes A, C, and E_Y for different values of Y size

The dipole modes A, C, and E_X (E_R) are redshifted with increasing X and R values. This is attributed to the fact that an increase in the values of R and X enhances the attraction between the meta-atoms, which weakens the repulsive force. The dipole modes A, C, and E_Y are blueshifted with increasing Y values. This phenomenon can be explained using the surface charge density. Figures S10(a)-(c) illustrate that the upper surface of the meta-atoms becomes increasingly negatively charged along the x -axis away from the endpoints of the incident light as the value of Y increases, leading to an increase in the repulsive force between the meta-atoms. Figures S10(d)-(h), instead, show that an increase in the value of Y causes a decrease in the charge at the ends of

the x -axis, resulting in a decrease in the attraction of the TD1 modes and an increase in the repulsive force. Both mechanisms essentially lead to the blueshift of the three dipole modes with increasing Y values.

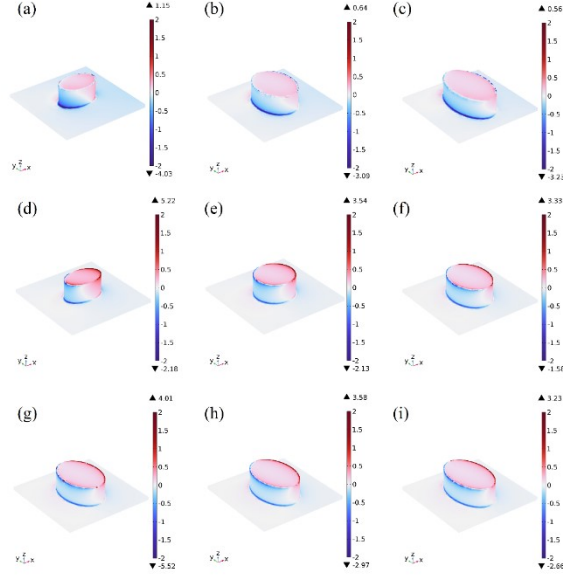


Figure S10. Surface charge density of mode A for (a) $Y = 2 \mu\text{m}$, (b) $Y = 4 \mu\text{m}$, and (c) $Y = 5 \mu\text{m}$. Surface charge density of mode C for (d) $Y = 2 \mu\text{m}$, (e) $Y = 3 \mu\text{m}$, and (f) $Y = 4 \mu\text{m}$. Surface charge density of mode E_Y for (a) $Y = 4.3 \mu\text{m}$, (b) $Y = 4.5 \mu\text{m}$, and (c) $Y = 4.75 \mu\text{m}$.

S11 Characterization of the absorption modes O and P

The location of the main absorption loss of mode O is consistent with that of mode C. However, the positional distribution of positive and negative charges on the upper surface of the meta-atom of mode O is opposite to that of mode C, and the magnetic resonance strength produced by current circuit **III** is stronger than that of circuits **I** and **II**. Modes A, C, and D gradually emerge and increase in strength as the height of the meta-atom increases.

Mode P has three current circuits, the same as in mode C, but the position of **I** and **II** are shifted from the side to the bottom of the meta-atom. The optical field is mainly localized at the four endpoints of the meta-atom.

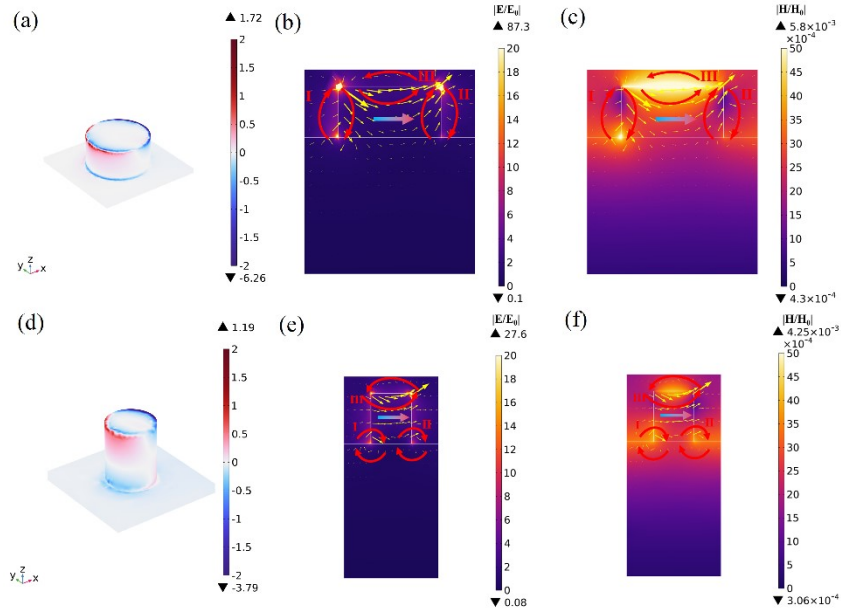


Figure S11. Characterization of the absorption modes O and P. (a) Surface charge density, (b) normalized optical field ($|E/E_0|$) and current density distribution in the x-z plane, and (c) normalized magnetic field ($|H/H_0|$) of mode O ($\lambda = 22.0 \mu\text{m}$) in 001ex direction with $P = 5 \mu\text{m}$. (d) Surface charge density, (e) normalized optical field ($|E/E_0|$) and current density distribution in the x-z plane, and (f) normalized magnetic field ($|H/H_0|$) of mode P ($\lambda = 16.0 \mu\text{m}$) in 001ex direction with $P_s = 0.4$.

S12 Surface charge density and normalized electric field distribution of mode A at different temperatures

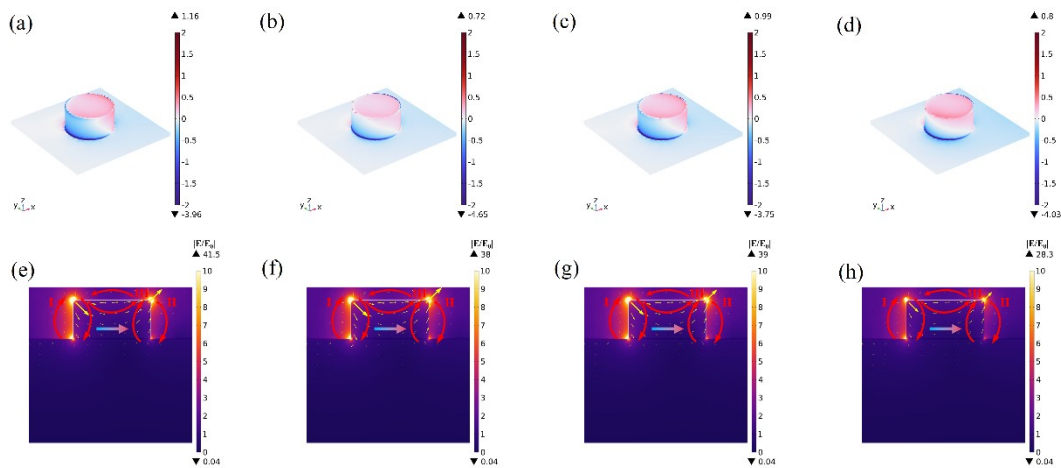


Figure S12. Surface charge density of mode A at (a) $T = 300 \text{ K}$, (b) $T = 395 \text{ K}$, (c) $T = 405 \text{ K}$, and (d) $T = 773 \text{ K}$. Normalized optical field ($|E/E_0|$) and current density

distribution in the x-z plane of mode A at (e) $T = 300$ K, (f) $T = 395$ K, (g) $T = 405$ K, and (h) $T = 773$ K.

S13 Contour map of absorption dependent on structural morphology at 20° oblique incidence angle in 100ey direction.

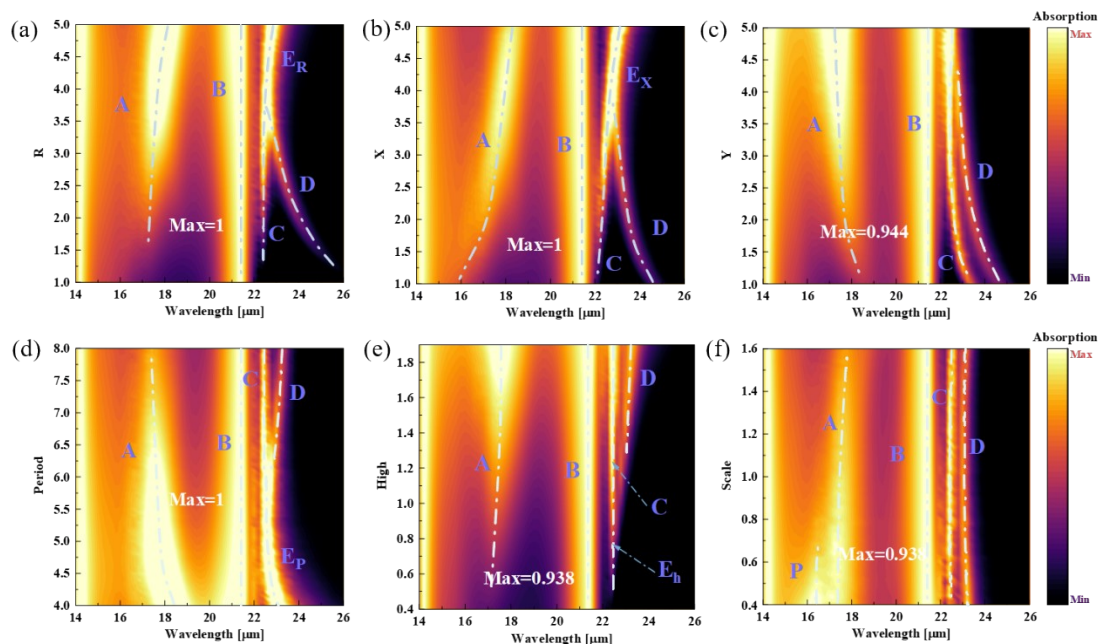


Figure S13. Contour map of absorption dependent on structural morphology at 20° oblique incidence angle. (a) Radius-dependent absorption contour map for metasurface. (b) X -dependent absorption contour map for metasurface. (c) Y -dependent absorption contour map for metasurface. (d) Period-dependent absorption contour map for metasurface. (e) Height-dependent absorption contour map for metasurface. (f) Scaling factor dependent absorption contour map for metasurface. The blue dotted line shows the variation of the absorbing mode with size. Blue letters mark the name of each absorption mode. White letters mark the maximum value of absorption in the contour plot.

S14 Contour map of absorption dependent on structural morphology at 20° oblique incidence angle in 100ez direction.

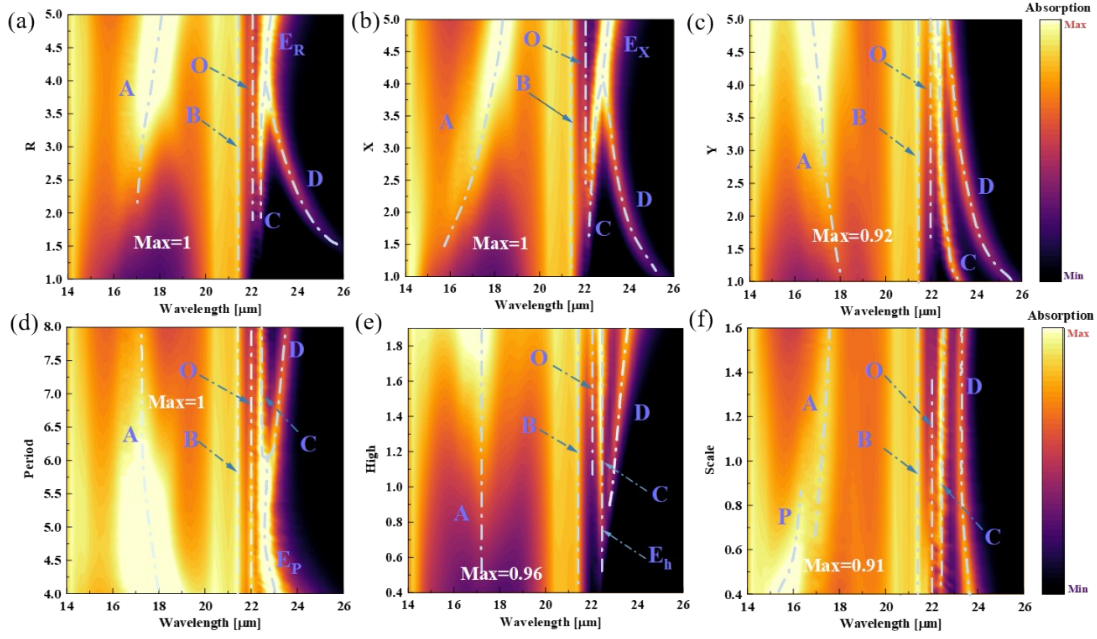


Figure S14. Contour map of absorption dependent on structural morphology at 20° oblique incidence angle. (a) Radius-dependent absorption contour map for metasurface. (b) X -dependent absorption contour map for metasurface. (c) Y -dependent absorption contour map for metasurface. (d) Period-dependent absorption contour map for metasurface. (e) Height-dependent absorption contour map for metasurface. (f) Scaling factor dependent absorption contour map for metasurface. The blue dotted line shows the variation of the absorbing mode with size. Blue letters mark the name of each absorption mode. White letters mark the maximum value of absorption in the contour plot.

S15 The positions of the different polarization modes as a function of the parameter

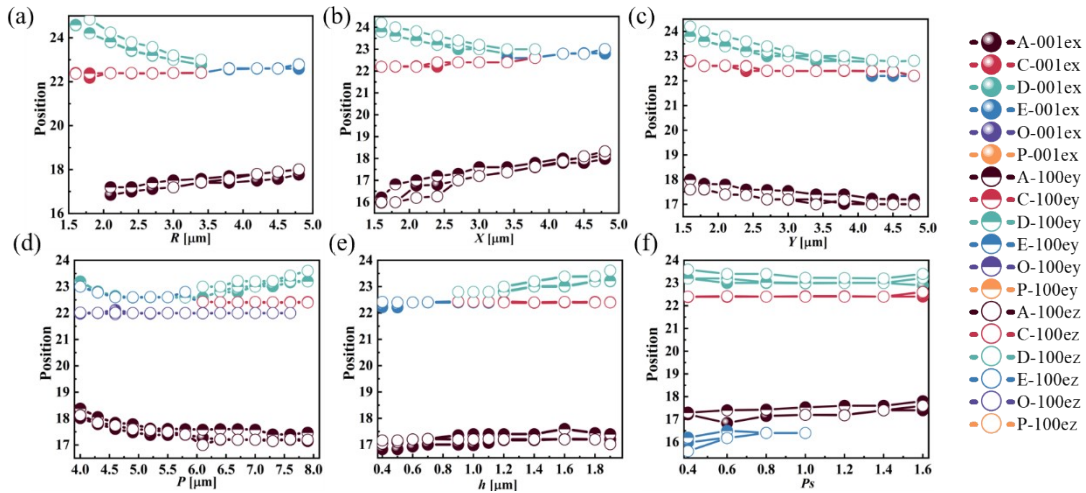


Figure S15. The positions of the different polarization modes as a function of the parameter (a) R , (b) X , (c) Y , (d) P , (e) h , (f) P_s . An example of the meaning of the legend: A-001ex indicates the change of mode A in the 100ex direction.

S16 Variation of spatial coherence of thermal emission from BTO metasurface with structural geometry

The angular distribution of the emissivity of the BTO in space is given in Figure S16. The spectral positions of the different polarization modes for each parameter used to calculate the spatial angular distribution are shown by Table S2. First, it can be seen that the spatial coherence is stronger in the 100ez direction than in the 001ex direction, i.e., the angular spread of the former is smaller than that of the latter. In addition, most of the parameters have larger angular spreads ($\text{fwhm} > 20^\circ$), which indicates poorer spatial coherence⁵. Moreover, the metasurface is not spatially coherent at all heights. However, increasing the value of P_s can significantly reduce the angular spread and thus increase the spatial coherence. Figure S17 supplements the spatial angular distribution for the remaining structural parameters, except that there is no spatial coherence, i.e., there are no complete spatial angles.

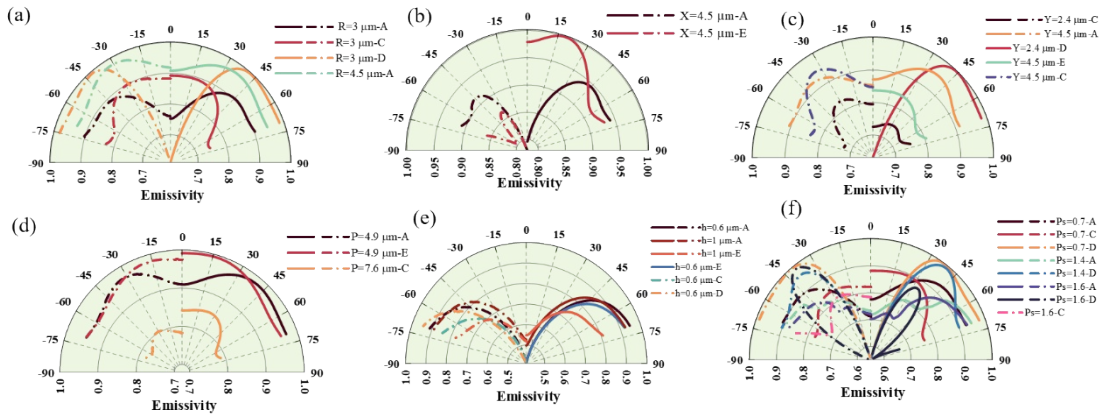


Figure S16. Spatial and spectral coherence of the BTO metasurfaces. Radiation patterns under the influence of parameter (a) R , (b) X , (c) Y , (d) P , (e) h and (f) P_s .

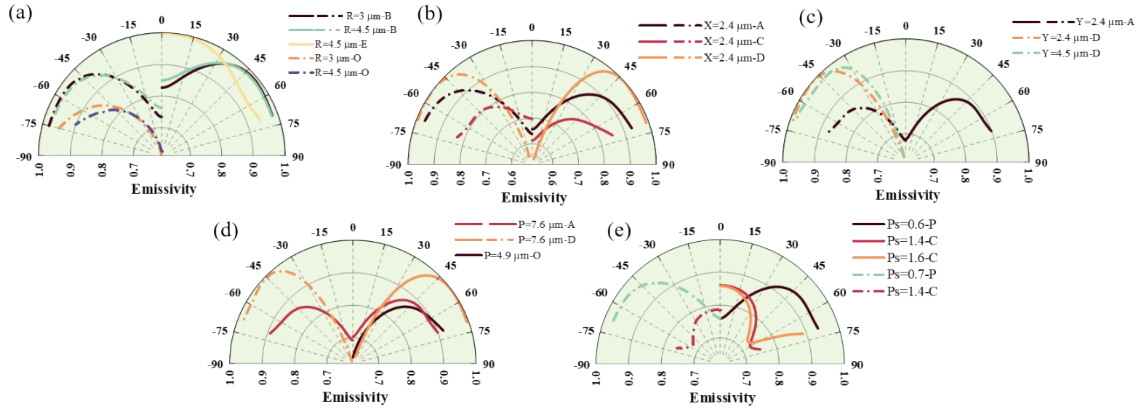


Figure S17. Spatial and spectral coherence of the BTO metasurfaces. Radiation patterns under the influence of parameter (a) R , (b) X , (c) Y , (d) P , and (e) P_s .

S17 Spatial angular distribution of the remaining supplementary structural parameters at $P_s = 1.6$.

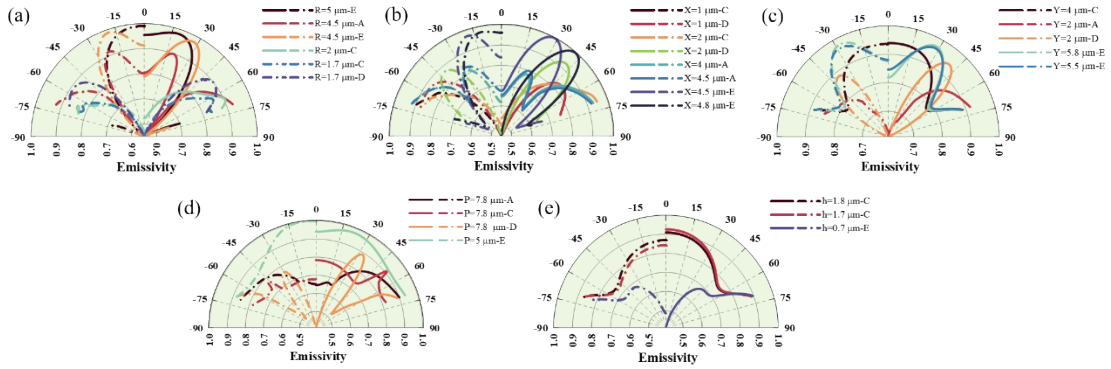


Figure S18. Spatial and spectral coherence of the BTO metasurfaces at $P_s = 1.6$.

Radiation patterns under the influence of parameter (a) R , (b) X , (c) Y , (d) P , and (e) h .

S18 The spectral positions of the different polarization modes for each parameter used to calculate the spatial angular distribution

Table S2 Spectral positions of individual polarization modes for different structural parameters at $P_s=1$ (default structural size)

Para	A-	B-	C-	D-	E-	P-	A-	B-	C-	D-	E-	P-	M-	O-
meter	00	00	00	00	00	00	10	10	10	10	10	10	10	10
s	1e	1e	1e	1e	1e	1e	0e							
($\mu\text{m}/\mu\text{m}$)	x	x	x	x	x	x	Z	Z	Z	Z	Z	Z	Z	Z

R=3	17.	21.	22.	23.		17.	21.	22.	23.		20.	22.
	2	4	4	0		2	4	4	2		4	0
R=4.	17.	21.			22.	17.	21.			22.	20.	22.
5	6	4			6	9	4			6	4	0
X=2.	16.		22.	23.		16.		22.	23.			
4	8		2	2		3		4	6			
X=4.	17.				22.	18.				22.		
5	8				8	1				8		
Y=2.	17.		22.	23.		17.		22.	23.			
4	4		4	2		4		6	6			
Y=4.	17.				22.	17.		22.	22.			
5	0				2	0		4	8			
P=4.9	17.				22.	17.				22.		
	4				6	6				6		
P=7.6	17.		22.	23.		17.		22.	23.			
	2		4	2		2		4	4			
H=0.	17.				22.	17.				22.		
6	0				4	2				4		
H=1	17.				22.	17.		22.	22.			
	0				4	2		4	8			
Ps=0.	16.		22.	23.		16.		22.	23.			16.
6	8		4	0		2		4	4			2
Ps=0.	17.		22.	23.				22.	23.			16.
7	0		4	0				4	4			2
Ps=1.	17.		22.	23.		17.		22.	23.			
4	4		4	0		4		4	2			
Ps=1.	17.		22.	23.		17.		22.	23.			
6	4		4	0		6		6	2			

Table S3 Spectral positions of individual polarization modes for different structural parameters at $P_s=1.6$

Parameters ($\mu\text{m}/\mu\text{m}$)	A- 001ex	C- 001ex	D- 001ex	E- 001ex	A- 100ez	C- 100ez	D- 100ez	E- 100ez
R=1.5		22.4				22.4		
R=1.7		22.4	24.0			22.4	24.4	
R=2		22.4	23.6			22.4	24.0	
R=4	18.2			22.8	18.5			22.8
R=4.5	18.2			22.8	18.6			22.8
R=5				22.8				22.8
X=1		22.2	23.8				24.6	
X=2		22.4	23.4			22.2	23.6	
X=4	18.2			22.9	18.8			23.0
X=4.5	18.4			23.0	18.8			23.0
X=4.8				23.2				23.0
Y=2	17.7	22.6	23.4		17.8	22.8	23.6	
Y=4	17.4	22.4	22.8		17.4	22.4	23.0	
Y=5.5				22.4			22.8	
Y=5.8				22.4				22.4
Y=6				22.4				22.4
P=5				22.6				22.6
P=5.5				22.6				22.6
P=7.8	17.4	22.4	23.4		17.6	22.4	23.6	
P=8	17.4	22.4	23.4		17.6	22.4	23.6	
H=0.7				22.4				22.6
H=1				22.4				22.6
H=1.7	17.6	22.4	23.2		17.6	22.4	23.4	
H=1.8	17.6	22.4	23.4		17.6	22.4	23.6	

S19 The angular spreads for each mode at different structural parameters

Table S4 angular spreads of individual polarization modes for different structural parameters at $P_s=1.6$. The letter "none" indicates that no spatial angle exists.

Paramet ers	A- 001ex	C- 001ex	D- 001ex	E- 001ex	A- 100ez	C- 100ez	D- 100ez	E- 100ez
($\mu\text{m}/^\circ$)								
R=1.5		4.47				3.47		
R=1.7		5.8	37.49			3.96	36.56	
R=2		5.84	36.8			4.11	38.08	
R=4	17.335			31.76	20.047			30.41
R=4.5	17.93			31.12	19.845			30.98
								6
R=5				30.26				none
X=1		none	37.00				none	
X=2		none	35.60			none	37.47	
X=4	17.3			31.38	20.02			31.75
X=4.5	17.75			31.64	20.85			29.90
X=4.8				33.63				26.89
				2				
Y=2	none		37.12		none	none	none	
Y=4	15.53	none	26.59		14.79	none	33.836	
Y=5.5				28.36				29.75
Y=5.8				28.13				29.17
Y=6				27.89				29.24
P=5				28.07				21.91
				1				3
P=5.5				28.27				25.84
				6				
P=7.8	8.126	2.6	22.65		none	3.6	25.71	

P=8	7.47	2.317	20.66	none	3.57	23.58
H=0.7				none		none
H=1				none		26.47
H=1.7	15.25	none	35.46	14.86&	none	
				17.22		
H=1.8	16.252	none	38.43	12.93&	none	39.48
				16.17		

Reference

1. I. Pasuk, F. Neațu, Ș. Neațu, M. Florea, C. M. Istrate, I. Pintilie and L. Pintilie, *Nanomaterials*, 2021, **11**, 1121.
2. A. A. Thanki and R. K. Goyal, *Mater. Chem. Phys.*, 2016, **183**, 447-456.
3. S. C. Kehr, M. Cebula, O. Mieth, T. Härtling, J. Seidel, S. Grafström, L. M. Eng, S. Winnerl, D. Stehr and M. Helm, *Phys. Rev. Lett.*, 2008, **100**, 256403.
4. M. Luo, D. Sun, N. Sun, Y. Hu, K. Zhang, D. Wang, Y. Li, B. Xing, Y. Xu and D. Wu, *Opt. Lett.*, 2019, **44**, 4215-4218.
5. J.-J. Greffet, R. Carminati, K. Joulain, J.-P. Mulet, S. Mainguy and Y. Chen, *Nature*, 2002, **416**, 61-64.